energies

MDPI

Article

Numerical Investigation on the Flow Characteristics in Axial-Inlet Cover-Plate Cavities

Zengyan Lian [1,2,3], Pei Wang [1,2,3,4,*], Guang Liu [1,2,3,4,*], Ziyi Sun [1,2,3], Jun Liu [1,2,3,4], Huiping Pei [1,2,3], Wenying Ju [1,2,3] and Xingen Lu [1,2,3]

[1] Key Laboratory of Light-Duty Gas-Turbine, Institute of Engineering Thermophysics, Chinese Academy of Sciences, Beijing 100190, China; lianzengyan@iet.cn (Z.L.); sunziyi@iet.cn (Z.S.); liujun@iet.cn (J.L.); peihuiping@iet.cn (H.P.); juwenying@iet.cn (W.J.); luxingen@iet.cn (X.L.)
[2] University of Chinese Academy of Sciences, Beijing 100049, China
[3] National Key Laboratory of Science and Technology on Advanced Light-Duty Gas-Turbine, Beijing 100190, China
[4] Qingdao Institute of Aeronautical Technology, Qingdao 266500, China
* Correspondence: wangpei@iet.cn (P.W.); liuguang@iet.cn (G.L.)

Abstract

This paper investigates the complex flow characteristics and parameter prediction methods for axial-inlet cover-plate cavities in pre-swirl systems numerically. Using a full-annulus three-dimensional computational model, the flow mechanisms of cover-plate cavities are compared between axial and radial inlet configurations. The analysis reveals that the axial-inlet configuration exhibits intensified non-axisymmetric vortex pairs in the low-radius region due to axial inflow inertia. These vortex structures enhance radial angular momentum exchange, leading to a substantial inlet angular momentum deficit that consequently reduces swirl ratios and pressure coefficients relative to the radial-inlet configuration. Furthermore, parametric studies demonstrate that small gap ratio amplifies circumferential flow non-uniformity through strong impingement effects, while elevated inlet swirl ratio significantly extends the source region boundary by strengthening centrifugal forces. To address the prediction discrepancies in existing models, this work proposes a modified correlation for the effective inlet swirl ratio that account for the inlet momentum loss and develops a new predictive model for the edge of source region incorporating centrifugal effects. These physics-based corrections, validated against simulation data, significantly improve the prediction accuracy for axial-inlet cover-plate cavities compared to conventional models.

Keywords: gas turbine; pre-swirl system; cover-plate cavity; prediction model

Check for updates

Academic Editor: Simone Salvadori

Received: 8 December 2025
Revised: 14 January 2026
Accepted: 15 January 2026
Published: 4 February 2026

Copyright: © 2026 by the authors. Licensee MDPI, Basel, Switzerland. This article is an open access article distributed under the terms and conditions of the Creative Commons Attribution (CC BY) license.

1. Introduction

With the continuous increase in turbine inlet temperature in advanced gas turbine design, turbine rotors are facing severe thermal load challenges, placing higher demands on efficient cooling techniques [1,2]. The cooling air to the turbine rotors is supplied by the pre-swirl system, in which the cover-plate cavity—formed between the cover-plate and the turbine disk—functions as the critical conduit for delivering cooling air to the rotor. The flow characteristics within the cover-plate cavity directly determine the pressure and relative temperature of the cooling air reaching the turbine rotor, thereby critically influencing both the cooling effectiveness of the turbine rotor and the overall engine

performance [3,4]. Therefore, a comprehensive understanding of these flow mechanisms is crucial for pre-swirl system design.

The cover-plate cavity is typically simplified as a rotating cavity with radial outflow, which can be categorized into the radial-inlet and the axial-inlet configurations. Based on theoretical and experimental methods, Morse et al. [5,6] established that the internal flow structure within a turbine cover-plate cavity could be divided into a source region, an Ekman layer, a sink region, and an internal core region. The source region normally occupies a substantial volume of the cavity [7]. Karabay et al. [8] further demonstrated that the extent of the source region (x_e) was primarily influenced by the non-dimensional flow rate coefficient (C_w) and the rotational Reynolds number (Re_φ). Their study quantified that x_e increases with the increasing C_w while decreases with the increasing Re_φ, leading to the development of empirical correlations to describe these relationships.

Existing research has primarily focused on the internal flow characteristics of radial-inlet cover-plate cavities. Owen et al. [9] experimentally confirmed that the flow within the source region adheres to the free-vortex law, under which the swirl ratio (β) decreases with the increasing radius (r) under the principle of angular momentum conservation. Consequently, the pressure coefficient (C_p) increases radially outward and exhibits positive correlation with β. Furthermore, they identified for a radial-inlet cover-plate cavity with pre-swirled inflow at inlet swirl ratio $\beta_{in} > 1$, recirculating vortex structures in the low-radius region induce an angular momentum deficit [10]. This deficit significantly alters the radial distribution of β. To account for this effect, the authors introduced an effective inlet swirl ratio (β_{eff}) to correct for the inlet momentum loss in predictive models.

However, the flow characteristics in axial-inlet cover-plate cavities are considerably more complex than those in radial-inlet configurations, primarily due to the significant axial velocity component—a feature distinct from radial-inlet flows dominated by circumferential motion. Experimental studies have highlighted key distinguishing features: Pilbrow et al. [11] reported a notable discrepancy between the measured radial distribution of the swirl ratio (β) and predictions using the effective inlet swirl ratio (β_{eff}), which was attributed to intense angular momentum deficit at the axial-inlet section; Pincombe et al. [12–15] observed non-axisymmetric flow fluctuations in the core region, indicating inherent flow instability within the source region; Iacovides et al. [16] noted asymmetric outlet pressure distributions induced by the coupling of axial and circumferential velocity components, for which no predictive correlations have yet been established; and Hsieh et al. [17] revealed that jet-to-disk separation distance (a critical geometric parameter) significantly modulates vortex development, with larger distances promoting the growth of inertia-driven vortices. Complementary computational investigations have further elucidated the flow dynamics: Tan et al. [18] demonstrated that RANS and LES offer complementary insights (LES resolving fine-scale transients, RANS reproducing mean flow structures); Dweik et al. [19] identified that axial inflow-rotating disk interactions induce complex vortex pair structures sensitive to key operating parameters; and Diogo et al. [20] confirmed that axial throughflow intensity triggers a transition from stable core flow to oscillatory motion beyond a critical flow coefficient— a phenomenon unique to axial-inlet configurations.

Currently, for axial-inlet cover-plate cavities, the complex flow behaviors and more pronounced angular momentum deficit (relative to radial-inlet counterparts) have been documented. However, the flow mechanisms at the inlet section and their influence on the flow parameters (such as β-r, C_p-r) have not been thoroughly investigated, leading to an absence of accurate correction methods for estimating flow parameters in axial-inlet cover-plate cavities. Therefore, this study employs a comprehensive numerical approach to investigate the flow characteristics of axial-inlet cavities. Through systematic comparison of flow structures and parameter distributions between axial and radial-inlet configurations,

this work aims to (1) identify the key drivers of enhanced angular momentum loss and vortex complexity in axial-inlet configurations. (2) elucidate quantitative impacts of β_{in}, C_w, and G on flow distribution in axial-inlet cover-plate cavities. (3) develop a refined predictive model specifically for estimating flow parameters in axial-inlet cover-plate cavities.

2. Model and Method

Based on the typical geometry of gas turbine cover-plate cavities, a simplified model of an axial-inlet cover-plate cavity is established, as shown in Figure 1. The integrated rotating components of the pre-swirl system, including the rotor disk and the cover plate coupled to the rotor, were simplified into a pair of co-rotating disks, with both the upstream and downstream disks defined as rotating walls. The cavity inlet was simplified as a uniform axial inlet annulus that accommodates the pre-swirled airflow from the pre-swirl nozzles, while the circumferentially distributed discrete cooling holes at the cavity outlet were simplified to a continuous radial outlet. The basic parameters and corresponding values of the cavity include: an inlet radius r_1 = 80 mm, an outlet radius b = 250 mm, and an axial inlet height a = 10 mm. The outlet width of cavity is s_c = 2 mm. The axial disk spacing s is set to different widths: 12.5 mm, 25 mm, and 37.5 mm, resulting in dimensionless gap ratios G = s/b = 0.05~0.15.

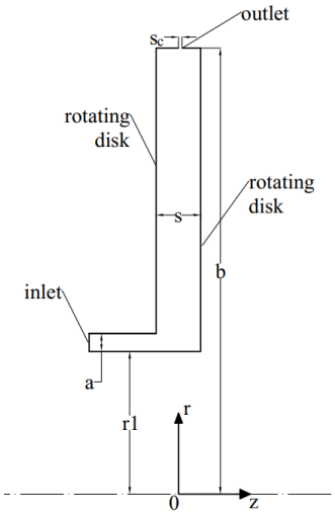


Figure 1. The simplified model of an axial-inlet cover-plate cavity.

To capture the complex three-dimensional flow structures and potential circumferential non-uniform flow parameters inside the axial-inlet cover-plate cavity, a full 360° annulus model [21–24] is employed. For the annular computational domain, a structured grid with an O-type topology is specifically generated to adapt to the annular circular geometry, as shown in Figure 2. Additionally, local mesh refinement was performed near all solid walls (within the boundary layer regions) with a target y^+ value of approximately 1 to accurately resolve the near-wall flow behaviors. The steady-state Reynolds-averaged Navier–Stokes (RANS) equations were solved using ANSYS CFX 19.0.

First, a grid independence test is conducted using meshes with 1.5 million, 2.5 million, and 3.5 million cells. As illustrated in Figure 3, the radial distributions of the swirl ratio obtained from the 2.5-million and 3.5-million-cell models show excellent agreement. The maximum relative difference between these two grids across all monitored locations is less than 1.3%, confirming that the solution is essentially independent of further mesh refinement. Therefore, the 2.5-million-cell model is selected for all subsequent simulations, as it provides an optimal balance between computational accuracy and cost.

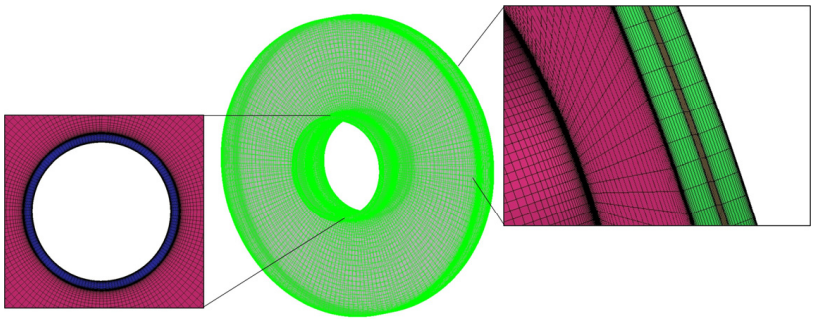


Figure 2. Structured mesh with O-grid topology for the full annulus model.

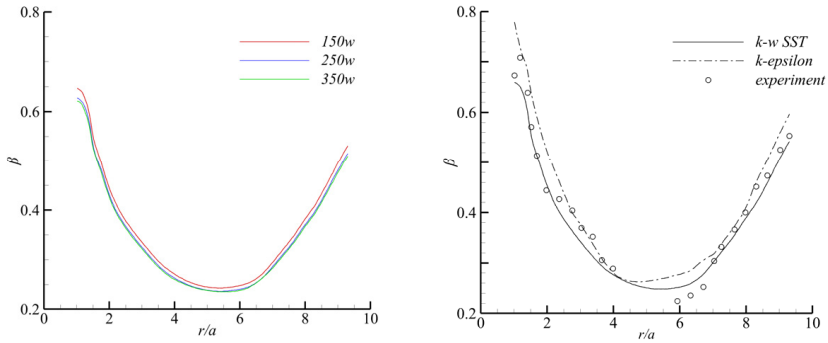


Figure 3. Grid independence test and comparison with experimental results: (**a**) Grid independence test; (**b**) Comparison with experimental data.

Then, the numerical method is validated against the experimental data of Owen et al. [25] for an axial-inlet cover-plate cavity. The experimental cavity comprised two disks of outer radius b = 190 mm, and a cylindrical shroud. The disk was attached at its inner diameter to a stainless-steel tube of inner radius a = 19 mm. The axial spacing between the two disks was s = 50 mm. The whole disk assembly could be rotated at Ω = 2600 rpm by an electric rotor. Figure 3b shows the experimental data at non-dimensional mass flow rate C_w = 689.

Simulations are performed with different turbulence models, and the results were compared with the experimental data as shown in Figure 3b. It can be found that the simulation results obtained with the k–ω SST turbulence model showed good agreement with the experimental data; however, the simulation results using k-epsilon turbulence model overpredicted the swirl ratio β especially in the low-radius region. This is because k–ω SST turbulence model can accurately calculate the flow separation [26–28] occurring at axial inlet region, which leads to the reduction in β in the low-radius region. Furthermore, the k–ω SST turbulence model has been demonstrated to accurately resolve the flow within the rotating disk cavity of pre-swirl systems [29,30]. Consequently, the k–ω SST turbulence model is adopted for this study.

3. Flow Characteristics in Cover-Plate Cavities with Different Inlet Configurations

To investigate the mechanism behind the significant different results observed experimentally between axial and radial inlet rotating cavities, numerical simulations are performed for both axial and radial inlet cover-plate cavities. For the operating conditions in this paper: the rotational speed is set to 8000 rpm ($Re_\varphi = 1.82 \times 10^6$, defined in Equation (1)) to simulate typical cover-plate cavity flow conditions of gas turbine (Re_φ typically falls within the range of 10^6–10^7), the non-dimensional mass flow coefficient C_w (given

by Equation (2)), which characterizes the throughflow rate relative to rotational effects, is often considerably large (C_w > 10,000) in cover-plate cavities to ensure an adequate supply of cooling air to the rotor; furthermore, the inlet swirl ratio β_{in} is generally greater than 1 as the cover-plate cavity is typically located downstream of a pre-swirl nozzle.

$$Re_\varphi = \frac{\rho \Omega b^2}{\mu} \tag{1}$$

$$C_w = \frac{\dot{m}}{\mu b} \tag{2}$$

First, under conditions of G = 0.1, C_w = 22,099, and β_{in} = 1.35, the flow in both axial and radial inlet cover-plate cavities are computed. The distributions of β and C_p along the radial direction at the axial mid-plane (z = 0) for both cavities are compared in Figure 4, where x represents the non-dimensional radius defined by Equation (3), and C_p represents the pressure coefficient defined by Equation (4) (where p is the local static pressure, p_1 is the inlet static pressure, ρ_1 is the inlet density, r_1 is the inlet radius, and Ω is the disk angular speed).

$$x = \frac{r}{b} \tag{3}$$

$$C_P = \frac{p - p_1}{0.5 * \rho_1 * \Omega^2 * r_1^2} \tag{4}$$

$$\beta = \beta_1 \left(\frac{r_1}{r}\right)^2 = \beta_1 \left(\frac{x_1}{x}\right)^2 \tag{5}$$

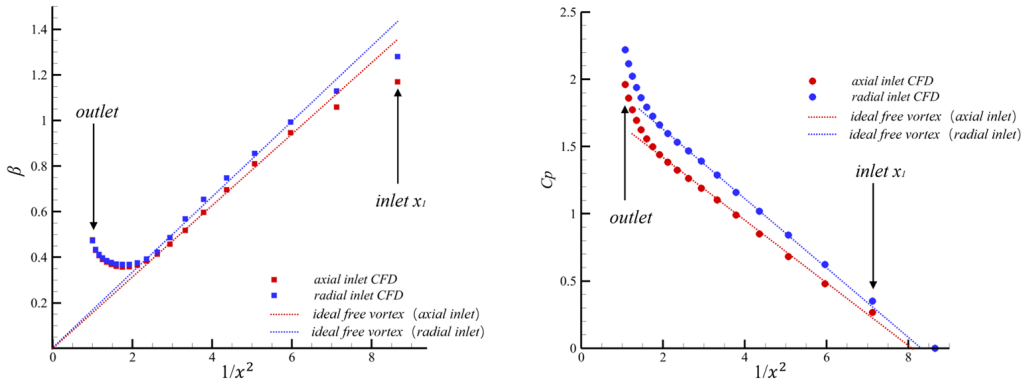


Figure 4. Simulation results of flow parameter distributions for axial and radial inlet cover-plate cavities (G = 0.1, C_w = 22,099, β_{in} = 1.35, z = 0): (**a**) distribution of β along radial direction; (**b**) distribution of C_p along radial direction.

In both axial and radial inlet cover-plate cavities, the swirl ratio β exhibits a linear relationship with $1/x^2$ over a certain radial extent from the inlet, consistent with the free-vortex law in the source region (Equation (5), where β_1 is the swirl ratio at x_1). Within the source region, β decays radially outward rapidly. Notably, under the same β_{in}, β within the source region are significantly lower in the axial-inlet cover-plate cavity than in the radial-inlet configuration. Beyond the source region, β increases with the radius due to the influence of the shroud, which accelerates the fluid via viscous shear. Since the shroud effect is similar for both configurations at the same C_w, the distributions of β converge in the high-radius region.

Both configurations exhibit a similar radial distribution profile of the pressure coefficient (C_p). However, the C_p magnitudes in the axial-inlet cover-plate cavity are notably

smaller. This difference can be explained by Equation (7)—derived by nondimensionalizing the simplified radial equilibrium equation (Equation (6), where V_Φ is the tangential velocity), which shows that the gradient of C_p versus $1/x^2$ is directly related to β_1. The axial-inlet configuration features a smaller β_1. Consequently, it produces a smaller radial pressure gradient, which leads to the observed reduction in overall C_p values.

$$\frac{dp}{dr} = \rho \frac{V_\Phi^2}{r} = \rho \beta^2 \omega^2 r \tag{6}$$

$$\frac{dc_p}{d(1/x^2)} = -\frac{\rho}{\rho_1} \beta_1^2 x_1^2 \tag{7}$$

The distinct flow parameter distributions observed between the axial and radial inlet configurations are primarily attributable to the difference in the inlet swirl ratio, β_1, as previously noted. Detailed analysis of the low-radius flow structure (Figure 5) reveals two recirculation vortices (A and B) in both cases. However, Vortex A is significantly larger in the axial-inlet cavity. The reason for the difference is that in the axial-inlet cover-plate cavity, the fluid passes through an axial section before turning radially outward. At this turning point, the initial axial momentum causes the flow to separate from the upstream disk, promoting the axial vorticity migration and the formation of a more extensive Vortex A. A similar Vortex B forms on the downstream disk but remains constrained to the corner by the impinging axial flow. This enhanced vortex structure intensifies the angular momentum exchange between high- and low-radius fluid, thereby reducing the net angular momentum at the inlet. As a result, the axial-inlet configuration exhibits more pronounced angular momentum decay, leading to the lower observed value of β_1.

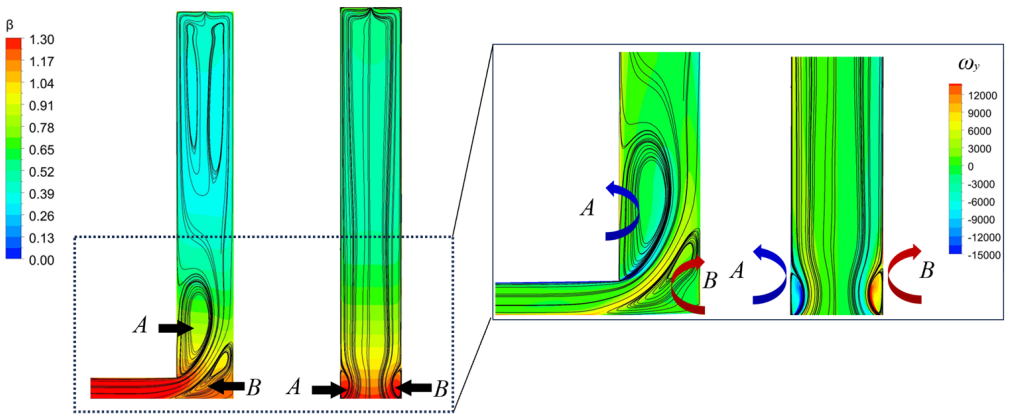


Figure 5. Comparison of flow structures between axial-inlet (**left**) and radial-inlet (**right**) configurations, visualized by streamlines with β and ω_z contours.

Further investigation reveals that when β_{in} is increased to 2, the flow in the axial-inlet cover-plate cavity develops distinct three-dimensional and asymmetric characteristics. Figure 6 shows that while the radial-inlet cover-plate cavity maintains circumferential symmetry, the axial-inlet cavity displays significant angular differences, where the maximum differences in β and C_p at the same radius reach 9.98% and 12.02%, respectively.

Figure 7 demonstrates that the flow field in the radial-inlet cover-plate cavity remains highly symmetric. In contrast, the axial-inlet cover-plate cavity exhibits different flow characteristics in the low-radius region, featuring two localized, large-scale vortex systems positioned approximately 180° apart azimuthally. This asymmetric vortex structure is attributed to the observed circumferential non-uniformity in the flow parameters.

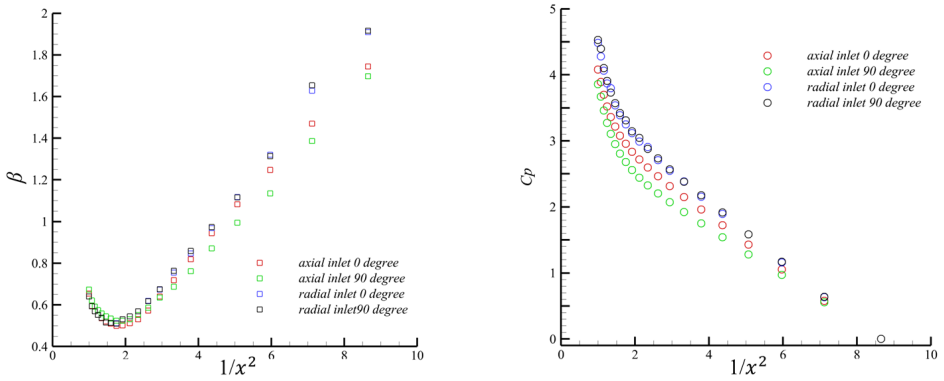


Figure 6. Flow parameter distributions at 0° and 90° degree (G = 0.1, C_w = 22,099, β_{in} = 2, z = 0): (**a**) distribution of β along radial direction; (**b**) distribution of C_p along radial direction.

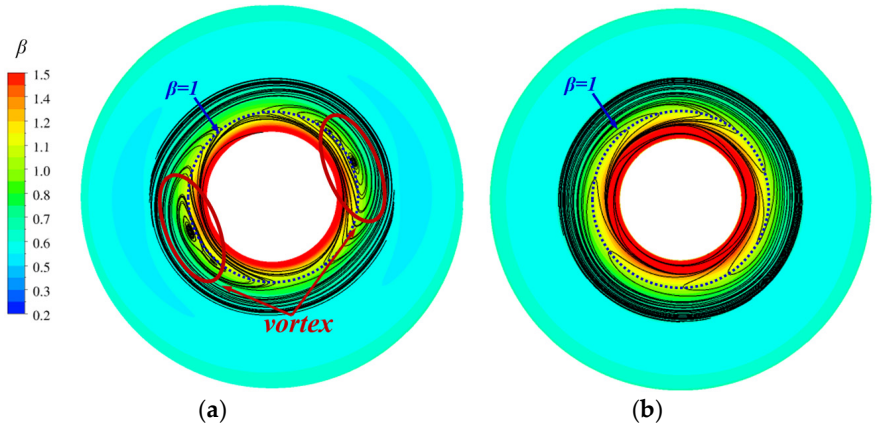


Figure 7. β contours and streamlines inside cover-plate cavities (G = 0.1, C_w = 22,099, β_{in} = 2, z = 0): (**a**) axial-inlet; (**b**) radial-inlet.

4. Flow Characteristics in an Axial-Inlet Cover-Plate Cavity

As mentioned above, axial-inlet cover-plate cavities exhibit significant different flow parameter distributions and three-dimensional flow effects compared to radial-inlet cover-plate cavities. Then, the mechanisms underlying these flow characteristics and their variation with key parameters are investigated in detail in this section.

4.1. Three-Dimensional Flow Characteristics

The simulations are performed at a rotational Reynolds number (Re_φ) of 1.82 × 10^6, with a non-dimensional flow rate coefficient (C_w) ranging from 11,045 to 44,199, an inlet swirl ratio (β_{in}) from 0.5 to 2.5, and gap ratios (G) of 0.05, 0.1, and 0.15. The vorticity distribution contours in Figures 8–10 reveal that the axial-inlet cover-plate configuration exhibits significant three-dimensional flow characteristics at the lowest flow rate (C_w = 11,045). As the mass flow rate increases, the flow uniformity improves because the inertial forces become dominant within the cavity. Furthermore, it is observed that a smaller G can amplify these three-dimensional effects.

When C_w = 11,045, distinct vortex structures are observed in the cover-plate cavities with gap ratios G = 0.05 and G =0.1. For G = 0.05, the vortex structures initiate at β_{in} = 1.35. Notably, the number of vortex structures increases with an increasing β_{in}: two vortices are present at β_{in} = 1.35, whereas three vortices form at β_{in} = 2. For G = 0.1, three-dimensional effects emerge at β_{in} = 2, with the vortex count also rising from two at β_{in} = 2 to four at β_{in} = 2.5.

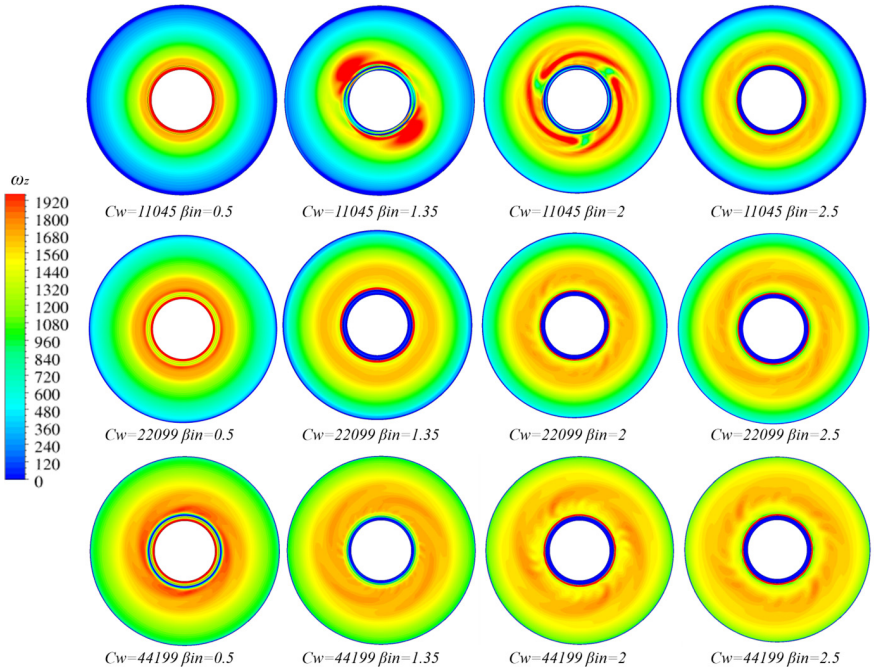


Figure 8. Vorticity contours on z = 0 plane for different β_{in}, C_w conditions (G = 0.05).

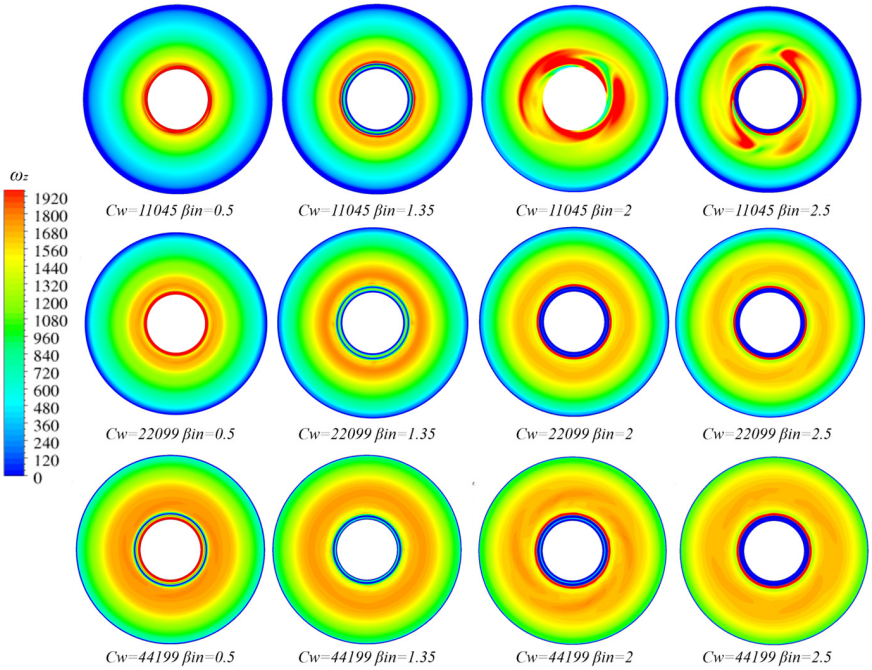


Figure 9. Vorticity contours on z = 0 plane for different β_{in}, C_w conditions (G = 0.1).

The vortex structures are predominantly distributed in the low-radius region, indicating that the vortex flow is induced by the cavity inflow. Under the influence of three-dimensional flow development, the case of G = 0.05 with βin = 1.35 exhibits the most pronounced asymmetric flow features. Specifically, the maximum differences in β and C_p at the same radial position reach 20.04% and 28.18%, respectively.

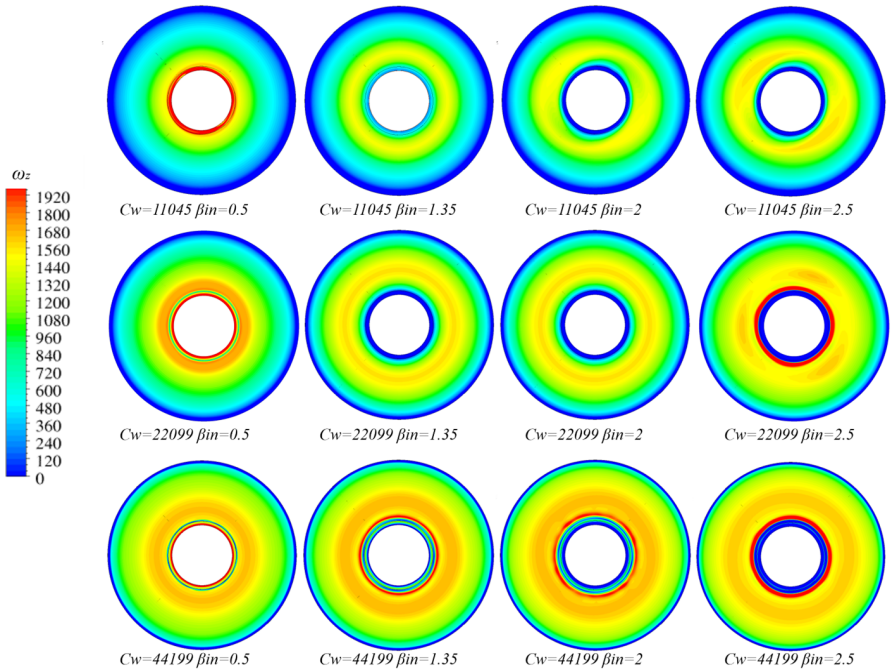


Figure 10. Vorticity contours on z = 0 plane for different β_{in}, C_w conditions (G = 0.15).

According to Equation (8), vorticity distribution depends on $\frac{\partial(rV_\Phi)}{\partial r}$ and $\frac{\partial V_r}{\partial \Phi}$. In the source region where angular momentum is conserved, $\frac{\partial(rV_\Phi)}{\partial r}$ can be neglected, which leads to $\omega_z \approx -\frac{1}{r}\frac{\partial V_r}{\partial \Phi}$.

$$\omega_z = \frac{1}{r}\left[\frac{\partial(rV_\Phi)}{\partial r} - \frac{\partial V_r}{\partial \Phi}\right] \quad (8)$$

As shown in Figure 11, the radial velocity gradient ($\frac{\partial V_r}{\partial \Phi}$) and the radial velocity (V_r) are circumferentially symmetric at large gap ratios. In contrast, at small gap ratios, a significant circumferential gradient develops, resulting in alternating regions of radial inflow and outflow that induce large-scale vortices. When the flow is radially inward, the resulting Coriolis force acts in the same direction as the disk rotation. Conversely, during radial outflow, the Coriolis force opposes the rotation. This opposing Coriolis force subsequently reinforces the flow instability, thereby sustaining the observed asymmetric vortex structure.

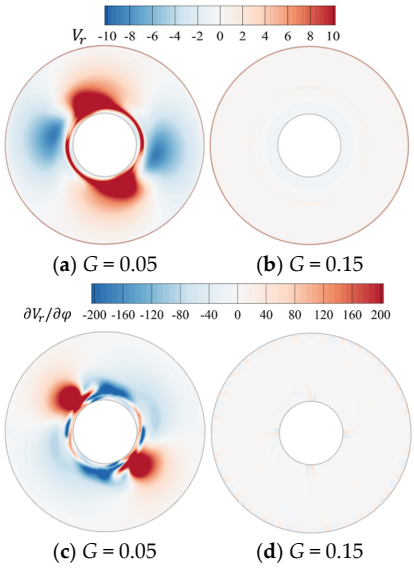
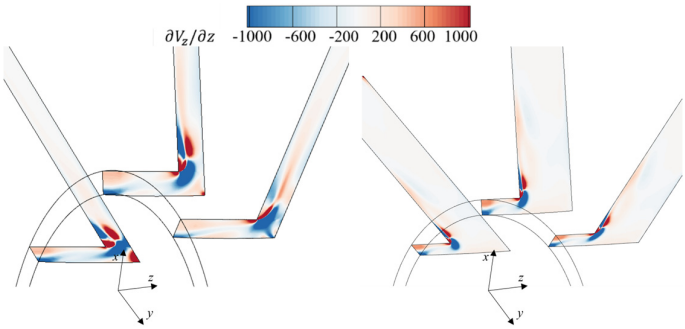


Figure 11. Contours of V_r and $\frac{\partial V_r}{\partial \Phi}$ on z = 0 plane with different G (C_w = 11,045, β_{in} = 1.35: (**a**,**b**) V_r, (**c**,**d**) $\frac{\partial V_r}{\partial \Phi}$).

The mechanism governing the uniformity of radial flow is further illustrated with reference to Figure 12: when the gap ratio (G) is small, the axial inflow promptly impinges on the downstream disk, thereby inducing significant flow disturbances and a pronounced non-uniform axial velocity gradient ($\frac{\partial V_z}{\partial z}$) in the low-radius region. Under such conditions, the fluctuations generated in the inlet region subsequently propagate into the radial flow, thereby compromising flow stability. In contrast, when the gap ratio is sufficiently large, the axial inflow is provided with sufficient space to develop, which effectively mitigates the impingement effect. As a result, the velocity distribution remains more uniform, thereby preserving the overall steadiness of the flow field. Due to the above significant three-dimensional phenomena, circumferentially averaged parameters are used for the subsequent analysis.



(**a**) G = 0.05 (**b**) G = 0.15

Figure 12. Contour of $\frac{\partial V_z}{\partial z}$ on z = 0 plane with different G (C_w = 11,045, β_{in} = 1.35).

4.2. Influence of Inlet Swirl Ratio

For a fixed gap ratio (G = 0.1) and coolant flow rate (C_w = 22,099), increasing the inlet swirl ratio (β_{in}) from 0.5 to 2.5 results in a corresponding rise in the local swirl ratio (β) within the low-radius region, as shown in Figure 13. However, the disparity between the local swirl ratio at x_1 (β_1, hollow squares) and the imposed inlet condition (β_{in}, solid squares) is amplified. In contrast, the outlet swirl ratio (β_b) remains relatively constant. Given that the radial pressure gradient is proportional to ${\beta_1}^2$, the pressure coefficient (C_p) increases significantly with β_{in}.

To elucidate the growing discrepancy between β_{in} and β_1, streamline patterns on the z-x plane are analyzed alongside contours of the swirl ratio (β) in Figure 14. The results indicate that a higher inlet swirl ratio (β_{in}) intensifies centrifugal forces, thereby expanding the recirculation vortices, especially vortex A. This enhanced vortex structure promotes greater angular momentum exchange between the core flow and the low-radius regions, which in turn amplifies the difference between the imposed inlet condition (β_{in}) and the local swirl ratio at x_1 (β_1).

The relative consistency of β_b is due to the similar shroud effect and the expansion of the edge of source region x_e. As β_{in} increases, the centrifugal pump effect expands the source region (where V_z = 0), as shown in Figure 13c, causing β to decay over a larger radius.

4.3. Influence of Flow Rate Coefficient

The effect of varying the non-dimensional flow rate coefficient (C_w) from 11,044 to 44,199 is investigated for a fixed gap ratio (G = 0.1) and inlet swirl ratio (β_{in} = 1.35), with the results presented in Figure 15. As C_w increases, the swirl ratio (β) within the source region remains largely unchanged. However, the outlet swirl ratio (β_b) decreases significantly. This reduction in outlet swirl ratio (β_b) correspondingly leads to a decrease in the pressure coefficient (C_p) in the high-radius region.

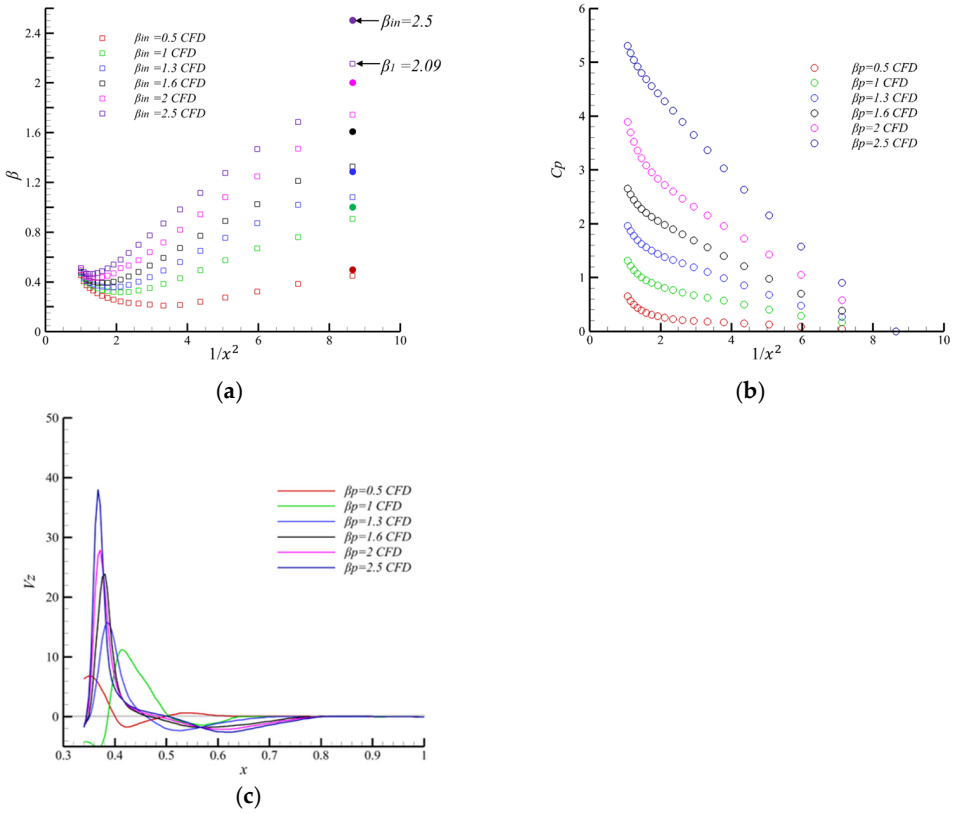


Figure 13. Distributions of circumferentially averaged flow parameters for different β_{in} (G = 0.1, C_w = 22,099, z = 0): (**a**) distribution of β along radial direction; (**b**) distribution of C_p along radial direction; (**c**) distribution of V_z along radial direction.

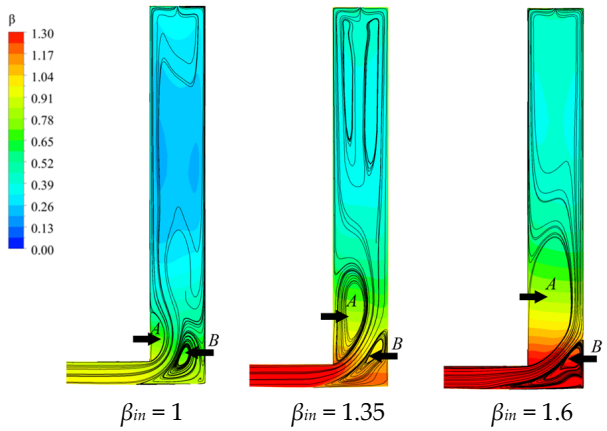


Figure 14. Streamline distributions for different β_{in} (G = 0.1, C_w = 22,099).

Figure 16 is obtained to further analyze the cause of these flow distribution characteristics. It is revealed that the overall extent of Vortex A and Vortex B remains largely unchanged with increasing C_w. The primary effect of C_w is a shift in the dominance between the vortices: a higher C_w strengthens the axial inertia, which enhances the upstream Vortex A while simultaneously suppressing the downstream Vortex B. Despite this shift, the angular momentum exchange at the inlet remains stable, resulting in a constant β_1. The observed decrease in the outlet swirl ratio (β_b) is attributed to two factors: (1) the expansion of x_e, which extends the region available for swirl decay, and (2) the relative weakening of the shroud's acceleration effect as the increase in the throughflow.

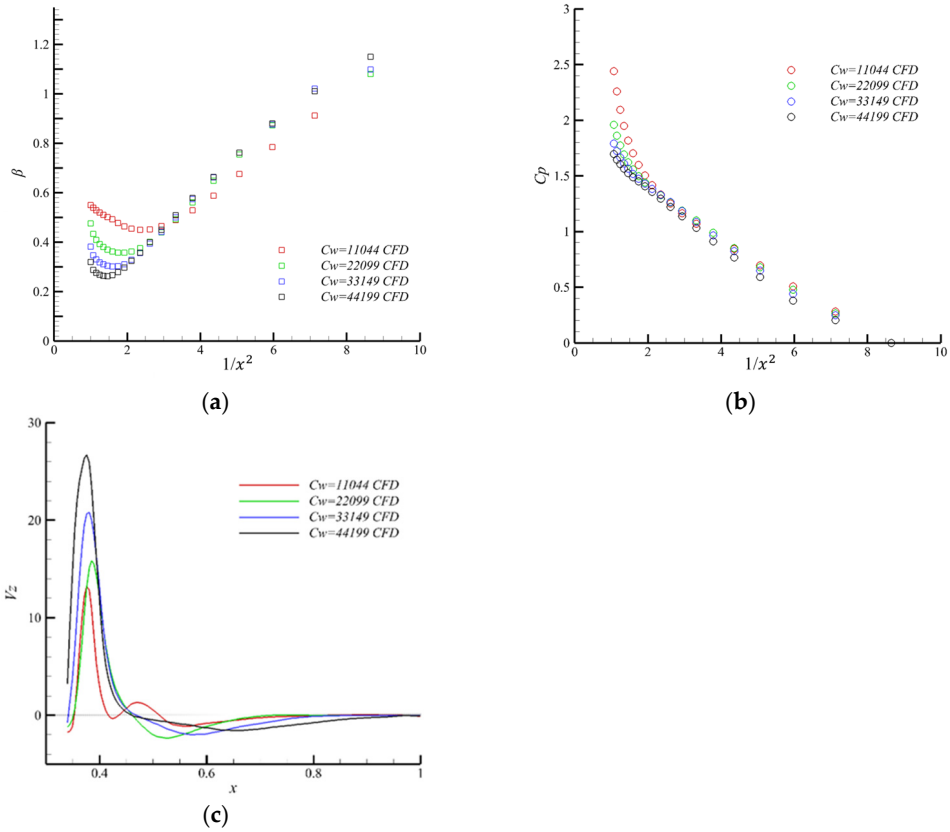


Figure 15. Distributions of circumferentially averaged flow parameters for different C_w (G = 0.1, β_{in} = 1.35, z = 0): (**a**) distribution of β along radial direction; (**b**) distribution of C_p along radial direction; (**c**) distribution of V_z along radial direction.

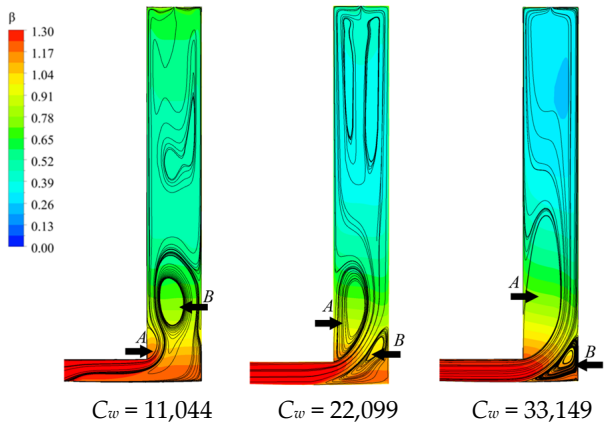


Figure 16. Streamline distributions for different C_w (G = 0.1, β_{in} = 1.35).

4.4. Influence of Gap Ratio

Simulations performed for gap ratios of G = 0.05, 0.1, and 0.15 (Figure 17) indicate that the gap ratio has an insignificant effect on the circumferentially averaged radial distributions of the outlet swirl ratio (β_b), the outlet pressure coefficient (C_{p_b}), and the edge of the source region (x_e). The primary influence of the gap ratio is instead manifested in the strength of the three-dimensional flow structures, as discussed previously, rather than in the circumferentially averaged parameters.

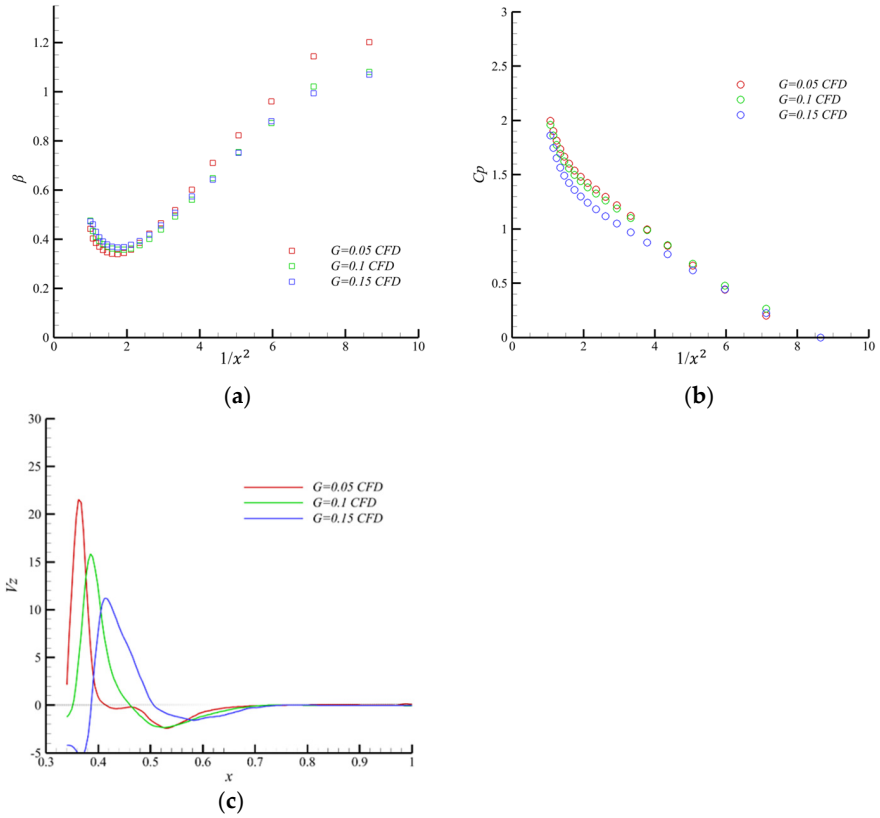


Figure 17. Distributions of circumferentially averaged flow parameters for different G (β_{in} = 1.35, C_w = 22,099, z = 0): (**a**) distribution of β along radial direction; (**b**) distribution of C_p along radial direction; (**c**) distribution of V_z along radial direction.

5. Flow Parameter Distribution Prediction Method

This study confirms that the flow in the source region generally obeys the free-vortex law, and the flow parameters along radial direction are significantly influenced by the local swirl ratio at x_1 (β_1). The existing model for radial-inlet cover-plate cavities employs an effective inlet swirl ratio (β_{eff}, Equation (9)) to account for angular momentum deficits at x_1. However, the direct application of this model to the axial-inlet configuration leads to an over-prediction of the swirl ratio (β), as illustrated in Figure 18. This discrepancy arises because angular momentum decay is more pronounced in the axial-inlet configuration due to its enhanced vortex structures.

$$\beta_{eff} = -0.043\beta_{in}^2 + 1.034\beta_{in} \quad (9)$$

Consequently, a new effective inlet swirl ratio, $\beta_{eff.ax}$, is defined to accurately predict the radial distribution of β in the axial-inlet configuration. This parameter is determined by extrapolating the linear region of the β versus $1/x^2$ profile within the source region back to the inlet location, based on numerical results across various β_{in} conditions. As summarized in Table 1, $\beta_{eff.ax}$ is consistently and significantly lower than the conventional β_{eff}, with the relative difference ranging from 5.30% to 9.91% for all β_{in} conditions.

Table 1. Comparison of $\beta_{eff.ax}$ and β_{eff} Under Different β_{in} Conditions.

β_{in}	$\beta_{eff.ax}$	β_{eff}	Difference
0.5	0.47	0.51	7.84%
1	0.92	0.99	7.07%

Table 1. *Cont.*

β_{in}	$\beta_{eff.ax}$	β_{eff}	Difference
1.35	1.25	1.32	5.30%
1.6	1.40	1.54	9.09%
2	1.75	1.90	7.89%
2.5	2.09	2.32	9.91%

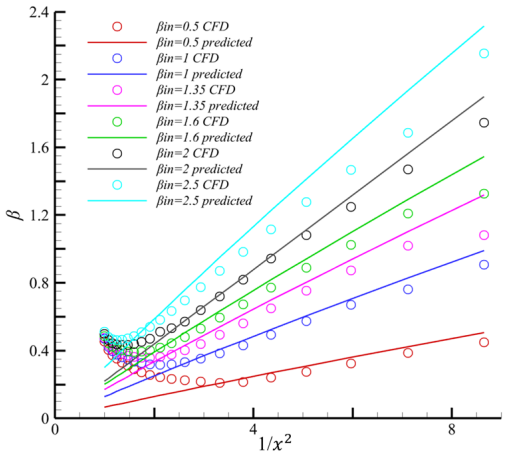


Figure 18. Comparison of distribution of β between CFD and prediction model using $\beta_1 = \beta_{eff}$.

It is assumed that the relationship between $\beta_{eff.ax}$ and β_{in} for axial-inlet cover-plate cavities also satisfies a quadratic polynomial of the form $\beta_{eff.ax} = -a{\beta_{in}}^2 + b\beta_{in}$. A fit to the data from Table 1 yields the coefficients $a = 0.0584$ and $b = 0.9843$, with a correlation coefficient of $R^2 = 0.9989$. The resulting empirical correlation for axial-inlet cavities is given by Equation (10). The predicted radial β distribution for the condition $G = 0.1$, $C_w = 22{,}099$, calculated using Equation (10), is plotted in Figure 19. The comparison demonstrates that utilizing $\beta_1 = \beta_{eff.ax}$ provides more accurate prediction of the flow parameter distribution in axial-inlet cover-plate cavities than the previous model shown in Figure 18.

$$\beta_{eff.ax} = -0.0584\beta_{in}^2 + 0.9989\beta_{in} \quad (10)$$

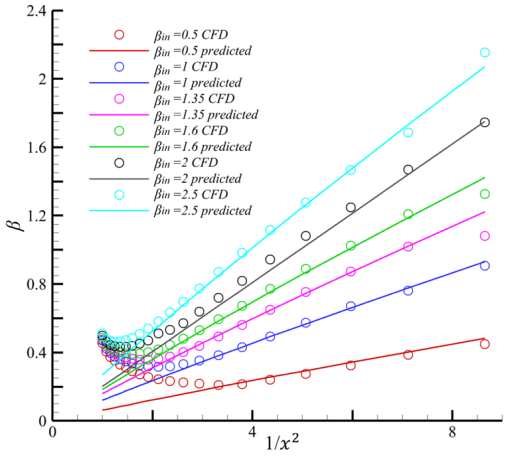


Figure 19. Comparison of distribution of β between CFD and prediction model using $\beta_1 = \beta_{eff.ax}$.

Furthermore, whereas the edge of the source region for a free disk ($x_{e.free}$) is typically a function of the non-dimensional mass flow rate (C_w) and rotational Reynolds number (Re_φ), as described by Equation (11), this study demonstrates that in axial-inlet cover-plate

cavities, $x_{e.ax}$ is also influenced by centrifugal force variations resulting from changes in the inlet swirl ratio (β_{in}). As β_{in} increases, the discrepancy between $x_{e.ax}$ and $x_{e.free}$ becomes more pronounced, as quantified in Table 2.

$$x_e = 1.375\left(C_W/\mathrm{Re}_\varphi^{0.8}\right)^{5/13} \tag{11}$$

$$x_{e.ax} = 0.4674\left(C_W/\mathrm{Re}_\varphi^{0.8}\right)^{0.5} - 0.2938e^{-\beta_{in}} + 0.7473 \tag{12}$$

Table 2. Numerical results for $x_{e.ax}$ under different conditions.

C_w	Re_φ	β_{in}	$x_{e.ax}$	$x_{e.free}$
22,099	1.82×10^6	0.5	0.7980	0.7639
22,099	1.82×10^6	1	0.8249	0.7639
22,099	1.82×10^6	1.35	0.9057	0.7639
22,099	1.82×10^6	1.6	0.9192	0.7639
22,099	1.82×10^6	2	0.9327	0.7639
22,099	1.82×10^6	2.5	0.9327	0.7639
11,044	1.82×10^6	1.35	0.8249	0.5850
33,149	1.82×10^6	1.35	0.9461	0.8928
44,199	1.82×10^6	1.35	0.9731	0.9772

Thus, an empirical correlation (Equation 12) incorporating β_{in} is derived, showing good agreement with simulation data (R^2 = 0.9431). The relationship between $x_{e.ax}$ and the parameters C_w, Re_φ, β_{in}, along with the confidence interval of the fit, is shown in Figure 20.

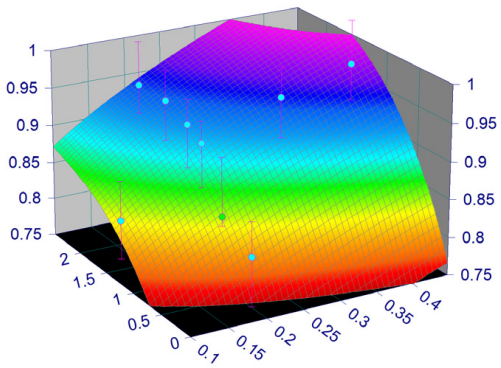


Figure 20. Variation in $x_{e.ax}$ with C_w, Re_φ, β_{in} and empirical correlation fit results.

6. Conclusions

In this study, the flow characteristics of an axial-inlet cover-plate cavity are investigated by numerical method with a full-annulus model. The main conclusions are as follows:

The flow characteristics of axial and radial inlet cover-plate cavities are compared. Both configurations exhibit a flow structure dominated by a source region, where the flow follows the free-vortex law. The main difference lies in the inlet region: the axial-inlet cover-plate cavity features larger vortex structures because of the axial inertia, and the enlargement of vortex scales further intensifies inlet angular momentum deficit.

The axial-inlet cover-plate cavity exhibits complex three-dimensional flow effects under certain conditions due to disturbances caused by the impingement of the flow on the downstream disk in the low-radius region, leading to circumferential non-uniformity in parameter distributions.

The variation in flow within axial-inlet cover-plate cavities under the influence of β_{in}, C_w, G is studied. Increasing β_{in} enhances the centrifugal force, which not only expands the inlet vortex structure but also widens the edge of source region ($x_{e.ax}$), thereby increasing outlet swirl ratio (β_b) and pressure coefficient (C_{p_b}). The increase in C_w enhances the inertial force, primarily influencing the competitive strength within the inlet vortex pair structures and reducing the shroud driving effect, then decreasing β_b and C_{p_b}. Gap Ratio (G) mainly affects flow stability. The decrease in G intensifies impingement disturbances, and further enhances the circumferential asymmetry.

Empirical correlations are developed for the edge of source region size ($x_{e.ax}$) and effective inlet swirl ratio ($\beta_{eff.ax}$) of axial-inlet cover-plate cavities, which are valid for the operating conditions with $\beta_{in} > 1$ and Re_φ within typical gas-turbine operating conditions. The proposed model characterizes the parameter distribution along radial direction in axial-inlet cover-plate cavities with much high accuracy.

The work presented in this paper substantially advances the fundamental understanding of swirling flow behaviors within cover-plate cavities. It elucidates the quantitative variation characteristics of cavity outlet pressure with respect to inlet flow parameters, and provides explicit guidance for the determination of key geometric parameters.

Author Contributions: Conceptualization, Z.L.; Methodology, Z.L.; Formal analysis, Z.S.; Investigation, Z.L. and G.L.; Resources, P.W. and G.L.; Data curation, G.L.; Writing—original draft, Z.L.; Writing—review & editing, P.W., J.L. and W.J.; Supervision, H.P. and X.L.; Project administration, H.P. and X.L. All authors have read and agreed to the published version of the manuscript.

Funding: The authors would like to acknowledge the financial support from the Strategic Priority Research Program of the Chinese Academy of Sciences (Grant No. XDC0140204) and the Strategic Priority Research Program of the Chinese Academy of Sciences (Grant No. XDB1280203).

Data Availability Statement: The original contributions presented in this study are included in the article. Further inquiries can be directed to the corresponding authors.

Conflicts of Interest: The authors declare no conflict of interest.

Nomenclature

$C_w = m/\mu b$	Nondimensional mass flow rate
$Re_\varphi = \rho\omega b^2/\mu$	Rotational Reynolds number
x_e	Nondimensional edge of source region
$x_{e.free}$	Nondimensional edge of source region of free disc
r	Radial coordinate
$\beta = V_\varphi/\omega r$	Swirl ratio
$C_p = (p\text{-}p_1)/0.5\rho_1\omega^2 {r_1}^2$	Pressure coefficient
C_{p_1}	Pressure coefficient at r_1
C_{p_b}	Pressure coefficient at b
β_{in}	Swirl ratio at inlet
β_1	Swirl ratio at r_1
β_b	Swirl ratio at b
β_{eff}	Effective swirl ratio of rotating cavity with radial inflow
$\beta_{eff.ax}$	Effective swirl ratio of rotating cavity with axial inflow
r_1	Inner radius of cavity
b	outer radius of cavity
a	Height of axial inlet
s_c	Axial width of outlet
s	Axial width of rotating cavity

$G = s/b$	Gap ratio
z	Axial coordinate
$x = r/b$	Nondimensional radial coordinate
p	Pressure
ρ	Density
Ω	Angular speed of disc
ω_z	Z component of vorticity
V_r	Radial velocity
V_Φ	Tangential velocity
V_z	Axial velocity
Φ	Tangential coordinate
e	Edge of source region
1	Inlet to cavity (at radial location)
b	outlet to cavity (at radial location)

References

1. Lewis, P.; Wilson, M.; Lock, G.D.; Owen, J.M. Effect of radial location of nozzles on performance of preswirl systems: A computational and theoretical study. *Proc. Inst. Mech. Eng. Part A J. Power Energy* **2008**, *223*, 179–190. [CrossRef]
2. Kusbeci, M.E.; Chew, J.W. Assessment of Wall-Modeled LES for Pre-Swirl Cooling Systems. In Proceedings of the Asme Turbo Expo: Turbomachinery Technical Conference and Exposition, Oslo, Norway, 11–15 June 2018.
3. Liu, G.; Gong, W.; Wu, H.; Lin, A. Experimental and CFD analysis on the pressure ratio and entropy increment in a cover-plate pre-swirl system of gas turbine engine. *Eng. Appl. Comput. Fluid Mech.* **2021**, *15*, 476–489. [CrossRef]
4. Liu, G.; Gong, W.; Wu, H.; Pang, L.; Lin, A. Theoretical and experimental evaluation of temperature drop and power consumption in a cover-plate pre-swirl system for gas turbine cooling. *Case Stud. Therm. Eng.* **2021**, *27*, 101221. [CrossRef]
5. Morse, A.P. Numerical Prediction of Turbulent Flow in Rotating Cavities. *J. Turbomach.* **1988**, *110*, 202–212. [CrossRef]
6. Iacovides, H. Turbulence modeling of axisymmetric flow inside rotating cavities. *Int. J. Heat Fluid Flow* **1991**, *12*, 2–11. [CrossRef]
7. Childs, P. *Rotating Flow*; Elsevier: Amsterdam, The Netherlands, 2010.
8. Karabay, H.; Chen, J.X.; Owen, J.M. Flow in a "cover-plate" preswirl rotor-stator system. *J. Turbomach.* **1999**, *121*, 160–166. [CrossRef]
9. Owen, J.M.; Rogers, R.H.; Pincombe, J.R. Source–sink flow inside a rotating cylindrical cavity. *J. Fluid Mech.* **1985**, *155*, 233–265. [CrossRef]
10. Karabay, H.; Wilson, M.; Owen, J.M. Predictions of effect of swirl on flow and heat transfer in a rotating cavity. *Int. J. Heat Fluid Flow* **2001**, *22*, 143–155. [CrossRef]
11. Karabay, H.; Pilbrow, R.; Wilson, M.; Owen, J.M. Performance of Pre-Swirl Rotating-Disk Systems. *J. Eng. Gas Turbines Power* **2000**, *122*, 442–450. [CrossRef]
12. Pincombe, J.R.; Owen, J.M. Vortex breakdown in a rotating cylindrical cavity. *J. Fluid Mech.* **1979**, *90*, 109–127. [CrossRef]
13. Viaud, B.; Serre, E.; Chomaz, J.M. The elephant mode between two rotating disks. *J. Fluid Mech.* **2008**, *598*, 451–464. [CrossRef]
14. Del Arco, E.C.; Maubert, P.; Randriamampianina, A.; Bontoux, P. Spatio—Temporal behaviour in a rotating annulus with a source—Sink flow. *J. Fluid Mech.* **2006**, *328*, 271–296. [CrossRef]
15. Martinand, D.; Serre, E.; Viaud, B. Instabilities and routes to turbulence in rotating disc boundary layers and cavities. *Philos. Trans. A Math. Phys. Eng. Sci.* **2023**, *381*, 20220135. [CrossRef] [PubMed]
16. Iacovides, H.; Chew, J.W. The computation of convective heat transfer in rotating cavities. *Int. J. Heat Fluid Flow* **1993**, *14*, 146–154. [CrossRef]
17. Hsieh, J.C.; Lin, T.F. Effects of jet-to-disk separation distance on the characteristics of mixed convective vortex flow in an impinging air jet confined in a cylindrical chamber. *Int. J. Heat Mass Transf.* **2005**, *48*, 511–525. [CrossRef]
18. Tan, Q.; Ren, J.; Jiang, H. Prediction of flow features in rotating cavities with axial throughflow by RANS and LES. In Proceedings of the Asme Turbo Expo: Power for Land, Sea, & Air, Orlando, FL, USA, 8–12 June 2009.
19. Dweik, Z.; Briley, R.; Swafford, T.; Hunt, B. Computational study of the heat transfer of the buoyancy-driven rotating cavity with axial throughflow of cooling air. In Proceedings of the Asme Turbo Expo: Power for Land, Sea, & Air, Orlando, FL, USA, 8–12 June 2009.
20. Pitz, D.B.; Chew, J.W.; Marxen, O. Effect of an axial throughflow on buoyancy-induced flow in a rotating cavity. *Int. J. Heat Fluid Flow* **2019**, *80*, 108468. [CrossRef]
21. Jakoby, R.; Zierer, T.; Lindblad, K.; Larsson, J. Numerical Simulation of the Unsteady Flow Field in an Axial Gas Turbine Rim Seal Configuration. In Proceedings of the Asme Turbo Expo: Power for Land, Sea, & Air, Vienna, Austria, 14–17 June 2004.

22. Mirzamoghadam, A.V.; Kanjiyani, S.; Riahi, A.; Vishnumolakala, R.; Gundeti, L. Unsteady 360 Computational Fluid Dynamics Validation of a Turbine Stage Mainstream/Disk Cavity Interaction. *J. Turbomach.* **2015**, *137*, 011008. [CrossRef]
23. Jackson, R.W.; Tang, H.; Scobie, J.A.; Owen, J.M.; Lock, G.D. Measurement of Heat Transfer and Flow Structures in a Closed Rotating Cavity. *J. Eng. Gas Turbines Power Trans. ASME* **2022**, *144*, 10. [CrossRef]
24. Li, J.; Li, X.; Ren, J. Flow and Heat Transfer in an Axial Throughflow Rotating Disk Cavity with Dual Inlets Under Variable Conditions. *Energies* **2025**, *18*, 4435. [CrossRef]
25. Owen, J.M.; Pincombe, J.R. Velocity Measurements Inside a Rotating Cylindrical Cavity with a Radial Outflow of Fluid. *J. Fluid Mech.* **1980**, *99*, 111–127. [CrossRef]
26. Ji, B.; Zhong, K.; Xiong, Q.; Qiu, P.; Zhang, X.; Wang, L. CFD Simulations of Aerodynamic Characteristics for the Three-blade NREL Phase VI Wind Turbine Model. *Energy* **2022**, *249*, 123670. [CrossRef]
27. DaSoghe, R.; Innocenti, L.; Andreini, A.; Poncet, S. Numerical Benchmark of Turbulence Modeling in Gas Turbine Rotor-Stator System. In Proceedings of the Asme Turbo Expo: Power for Land, Sea, & Air, Glasgow, UK, 14–18 June 2010.
28. Frączek, D.; Wroblewski, W. Heat Transfer Modelling in a Rotating Cavity Using the SST k-ω Turbulence Model. *Arch. Mech.* **2014**, *66*, 343–364.
29. Karnahl, J.; Wolfersdorf, J.V.; Tham, K.M.; Wilson, M.; Owen, J.M. CFD Simulations of Flow and Heat Transfer in a Pre-Swirl System: Influence of Rotating-Stationary Domain Interface. In Proceedings of the Asme Turbo Expo: Power for Land, Sea, & Air, Vancouver, BC, Canada, 6–10 June 2011.
30. Didenko, R.A.; Karelin, D.V.; Ievlev, D.G. Pre-Swirl Cooling Air Delivery System Performance Study. In Proceedings of the Asme Turbo Expo: Power for Land, Sea, & Air, Copenhagen, Denmark, 11–15 June 2012.

Disclaimer/Publisher's Note: The statements, opinions and data contained in all publications are solely those of the individual author(s) and contributor(s) and not of MDPI and/or the editor(s). MDPI and/or the editor(s) disclaim responsibility for any injury to people or property resulting from any ideas, methods, instructions or products referred to in the content.